AGU ADVANCING EARTH AND SPACE SCIENCES

JGR Space Physics

RESEARCH ARTICLE
10.1029/2025JA033820

Key Points:

- Distribution maps of whistler-mode wave amplitude are constructed to reveal the regions around the Moon favorable for wave generation
- Plasma parameters are evaluated for low- and high-energy electrons separately to understand their correlation with whistler-mode waves
- Magnetic field line connections with the Moon exhibit the highest positive correlation with temperature anisotropy of high-energy electrons

Supporting Information:

Supporting Information may be found in the online version of this article.

Correspondence to:

A. Prasad and W. Li,
abhi99@bu.edu;
wenli77@bu.edu

Citation:

Prasad, A., Li, W., Ma, Q., Shen, X.-C., Artemyev, A., Poppe, A. R., et al. (2025). Global survey of Whistler-mode waves in the lunar plasma environment: Insights from 11 years of ARTEMIS observations. *Journal of Geophysical Research: Space Physics*, *130*, e2025JA033820. https://doi.org/10.1029/2025JA033820

Received 6 FEB 2025
Accepted 19 MAY 2025

Global Survey of Whistler-Mode Waves in the Lunar Plasma Environment: Insights From 11 Years of ARTEMIS Observations

Abhinav Prasad[1], Wen Li[1], Qianli Ma[1,2], Xiao-Chen Shen[1], Anton Artemyev[3], Andrew R. Poppe[4], Yuki Harada[5], Murong Qin[1], Vassilis Angelopoulos[3], and Mei-Yun Lin[4]

[1]Center for Space Physics, Astronomy Department, Boston University, Boston, MA, USA, [2]Department of Atmospheric and Oceanic Sciences, University of California, Los Angeles, CA, USA, [3]Department of Earth, Planetary, and Space Sciences, University of California, Los Angeles, CA, USA, [4]Space Sciences Laboratory, University of California, Berkeley, CA, USA, [5]Department of Geophysics, Graduate School of Science, Kyoto University, Kyoto, Japan

Abstract Whistler-mode waves are among the most ubiquitously observed plasma waves in the vicinity of Earth's Moon, providing an important diagnostic tool for plasma processes. However, a complete understanding of key plasma parameters responsible for whistler-mode generation remains elusive. In this study, we conduct a comprehensive statistical survey using 11 years of in-situ measurements from the ARTEMIS mission to reveal the global distribution of whistler-mode wave amplitude and occurrence rate as the Moon traverses through the solar wind, magnetosheath, and magnetotail during a typical lunar orbit. Our findings reveal that the highest whistler-mode wave amplitudes are observed when the Moon crosses Earth's magnetosheath. A parametric study is conducted to explore the correlation between whistler-mode wave occurrence rate and plasma parameters such as electron temperature anisotropy and heat flux. These parameters are analyzed separately for low-energy (<100 eV) and high-energy (>100 eV) electrons. The results indicate that whistler-mode wave occurrence rates exhibit a stronger positive correlation with the temperature anisotropy of high-energy electrons compared to low-energy electrons. Moreover, the parallel heat flux (normalized by the free streaming heat flux) of high-energy electrons shows a moderate positive correlation with whistler-mode wave amplitude (normalized to the background magnetic field) in both the solar wind and magnetosheath regions. We further investigate the influence of the background magnetic field line connection to the lunar surface on whistler-mode waves. Overall, our analysis demonstrates that the temperature anisotropy of high-energy electrons has a higher positive correlation with magnetic field connection than that of low-energy electrons.

Plain Language Summary During a typical lunar orbit, Earth's Moon encounters a variety of transient plasma conditions as it traverses the solar wind and Earth's magnetosphere. As an unmagnetized planetary object, Moon consists of weak crustal magnetization on its surface which acts as hotspots for intense plasma activity. Whistler-mode waves, which are right-hand polarized electromagnetic waves observed between ion and electron gyrofrequencies, are frequently detected in the vicinity of the Moon. In this study, we conduct a statistical survey of whistler-mode wave distributions around the Moon and assess the critical plasma conditions favorable for their generation in lunar plasma environment. Our findings show that the strongest whistler-mode waves occur when the Moon passes through Earth's magnetosheath. We analyze potential plasma parameters, including electron temperature anisotropy and heat flux, categorically for low-energy (<100 eV) and high-energy (>100 eV) electron populations to evaluate their correlation with whistler-mode waves. The results indicate that the temperature anisotropy of high-energy electrons is most critical for whistler-mode wave generation across different plasma regions. This study highlights the importance of separately evaluating plasma parameters for low- and high-energy electrons to understand the electron population crucial for whistler-mode wave generation in different plasma regimes encountered during a lunar orbit.

1. Introduction

The Moon is an unmagnetized planetary object orbiting Earth at a distance of roughly 60 Earth radii (R_E), with a period of approximately 27.3 days. Its large orbital radius allows the Moon to spend a majority of time outside Earth's magnetosphere, exposing it to a variety of plasma regions, from the upstream solar wind to Earth's magnetotail (Halekas et al., 2011). Lacking a global magnetic field, the Moon features localized crustal magnetic field sources distributed throughout its surface, which allows transient plasma near the Moon to interact directly with the lunar surface, resulting in a number of interesting plasma waves and instabilities (Chu et al., 2021; Halekas et al., 2006, 2011, 2012; Harada & Halekas, 2016; Nakagawa, 2016). Among these different plasma waves, whistler-mode waves are the most frequently detected. These are right-hand polarized electromagnetic waves with frequencies between ion and electron gyrofrequencies (Halekas et al., 2006; Harada et al., 2015; Sawaguchi et al., 2022; Tong, Vasko, Artemyev, et al., 2019).

Previous studies have investigated the properties and generation mechanisms of whistler-mode waves in the lunar plasma environment, highlighting their various aspects. Harada et al. (2014, 2015) used linear wave growth calculations to show that the generation of whistler-mode waves around the Moon can be attributed to the pitch angle anisotropy of the local electron velocity distribution function (Gurnett & Bhattacharjee, 2017; Kennel, 1966). Harada et al. (2015) found that the generation of high-frequency (∼100 Hz) whistler-mode waves observed when the Moon traverses the solar wind is strongly dependent on the connectivity of the background magnetic field lines to the lunar surface. Sawaguchi et al. (2022) also reported a strong dependence of whistler-mode waves on the magnetic field line connection to the lunar surface. Electrons traveling along magnetic field lines connected to the lunar surface undergo processes such as magnetic reflection, backscattering, or surface absorption. These interactions lead to a loss cone formation in the electron velocity distribution, which enchances the growth rate of whistler-mode waves (Halekas et al., 2006, 2012; Harada et al., 2014; Tsugawa et al., 2011). On the anti-solar side of the Moon, the formation of the lunar wake creates an electric potential structure capable of reflecting electrons with low parallel velocities along magnetic field lines (Halekas, 2005; S. Xu et al., 2019; X. Xu et al., 2019; Zhang et al., 2014). This wake also develops E X B drifts, leading to the formation of a loss cone distribution that is favorable for the generation of whistler-mode waves (Fatemi et al., 2013; Halekas et al., 2002; Nakagawa & Iizima, 2005). Tong, Vasko, Artemyev, et al. (2019) conducted a statistical survey of quasi-parallel whistler-mode waves in the solar wind, finding that their amplitudes typically range from 10 to 100 pT. They also found a strong positive correlation between the occurrence rate of quasi-parallel whistler-mode waves in the solar wind and the temperature anisotropy of electrons between 10 eV and 24 keV, whereas wave amplitudes normalized by the total magnetic field show a strong positive correlation with the electron parallel plasma beta. Furthermore, Tong, Vasko, Pulupa et al. (2019) demonstrated that the generation of whistler-mode waves in the solar wind is strongly dependent on the temperature anisotropy of halo electron population, together with whistler heat flux instability due to the drifting core and halo electron population (Gary et al., 1994). Sawaguchi et al. (2021) explained the generation of whistler-mode chorus waves in the vicinity of the Moon using non-linear wave growth modeling (Omura, 2021; Omura et al., 2008).

Studying plasma waves around the Moon allows us to reveal important plasma properties that are difficult to resolve in time through in-situ measurements. Whistler-mode waves being one of the most frequently detected plasma waves around the Moon, play an important role in governing the overall plasma dynamics. With more than a decade of observational and theoretical studies, significant advances have been made in understanding whistler-mode waves around the Moon. However, several key aspects of whistler-mode waves in the vicinity of the Moon remain elusive. For instance, the global distribution of whistler-mode wave amplitudes across different regions of the lunar plasma environment is still not fully understood. Moreover, there is limited understanding of how the global whistler-mode wave distribution around the Moon varies in response to the transient plasma conditions encountered during a typical lunar orbit. The plasma parameters responsible for developing conditions conductive to whistler-mode wave generation in the lunar plasma environment have been explored when the Moon traverses the solar wind (Harada et al., 2015; Tong, Vasko, Artemyev, et al., 2019). However, a comprehensive understanding of the critical plasma parameters essential for whistler-mode wave generation when the Moon crosses Earth's magnetosheath and magnetotail remains lacking. Recent studies have highlighted that macroscopic plasma parameters alone often fail to fully capture the local pitch angle anisotropies in the electron velocity distribution function at kinetic scales, which are crucial for whistler-mode wave generation (Page et al., 2021; Tong, Vasko, Pulupa, et al., 2019). Magnetic field line connection to the lunar surface has been shown to play an important role in affecting local electron pitch angle anisotropy and whistler-mode wave growth rate when the Moon is in the solar wind (Harada et al., 2015). However, the question remains elusive regarding how field line connectivity correlates with local plasma conditions critical for whistler-mode wave generation in Earth's magnetosphere. In this study, we attempt to address these gaps and provide new insights into the properties and generation mechanisms of whistler-mode waves in the lunar plasma environment.

In this study, we use 11 years of in-situ observations from the Acceleration, Reconnection, Turbulence and Electrodynamics of the Moon's Interaction with the Sun (ARTEMIS) mission (V. Angelopoulos, 2011) to conduct a comprehensive statistical survey of whistler-mode wave amplitudes and occurrence rates across the various plasma regions encountered during a lunar orbit around the Earth. We also examine the potential plasma parameters responsible for whistler-mode wave generation, aiming to identify the key parameters with the highest positive correlation with whistler-mode wave amplitude and occurrence rates. Moreover, we calculate the plasma parameters for low- and high-energy electron populations separately, to determine the specific electron populations most relevant for whistler-mode wave generation in different plasma regions.

2. Data and Methodology

In this study, we use in-situ observations from the dual ARTEMIS probes collected between July 2011 and December 2022. Background magnetic field measurements are taken from the Fluxgate Magnetometer (FGM) (Auster et al., 2008), while high-frequency wave magnetic field measurements are sourced from the Search Coil Magnetometer (SCM) (Roux et al., 2008) aboard the ARTEMIS probes. The fast survey mode of SCM provides Fast Fourier Transform (FFT) magnetic spectra with a time resolution of 8 s, enabling the calculation of total magnetic power spectral density (PSD) by combining measurements parallel ($PSD_{\|}$) and perpendicular ($PSD_{\perp}$) to the spacecraft spin plane ($PSD = PSD_{\|} + 2\ PSD_{\perp}$). For particle moments and flux measurements, we use data from the Electrostatic Analyzer (ESA) (McFadden et al., 2008).

To identify high-frequency whistler-mode wave events, we use the total magnetic power spectral density from SCM. The magnetic spectra are initially cleaned to remove spike noise from instrumental sources by excluding data points with intensities greater than 1 nT^2/Hz. The cleaned magnetic spectra are used to identify whistler-mode wave events through the following three steps: (a) The magnetic spectra are divided into daily segments and a threshold intensity level is defined for each frequency channel as the 40th percentile of intensity measurements within that segment. Data points with intensities below four times the defined threshold values are removed for each frequency channel. (b) At each time step, the processed magnetic power spectra are checked for the presence of local peaks in magnetic intensity as a function of frequency, which is a typical characteristic of whistler-mode wave events (Sawaguchi et al., 2022). Magnetic spectra without any local intensity maxima are excluded from consideration as whistler-mode wave events. (c) The processed magnetic spectra at each time are used to identify whistler-mode wave events between 16 Hz and 0.8 f_{ce} (electron gyrofrequency). Events with maximum intensity at frequencies below 0.15 f_{ce} are excluded to avoid potential overlaps with other low-frequency wave modes. The magnetic spectra of whistler-mode wave events are then integrated over the specified frequency range (16 Hz–0.8 f_{ce}) to compute the whistler-mode wave amplitude.

Figure 1 shows examples of ARTEMIS observations when the Moon is located in the solar wind, magnetosheath, and magnetotail regions, as reflected by the energy spectrogram of ion energy flux (Panels b1–b3). The ion energy spectra in the magnetosheath region have a higher standard deviation around the solar wind proton energy (~835 eV), whereas the ion spectra in the solar wind region are narrowly peaked at the solar wind proton energy with a lower standard deviation. Panels h1–h3 show the magnetic spectra of whistler-mode wave events, filtered from total magnetic spectra (Panels g1–g3), using the method described earlier. Panels i1–i3 present the wave amplitudes calculated from the corresponding magnetic spectra of whistler-mode waves.

To determine the electron plasma parameters, we use the velocity distribution function (VDF) and corresponding particle moments for electrons up to 24 keV, obtained from the ESA instrument onboard ARTEMIS. Specifically, we calculate the electron temperature anisotropy ($T_{e\perp}/T_{e\|} - 1$) and the parallel heat flux (q_e). Here, $T_{e\|}$ and $T_{e\perp}$ represent the electron temperatures parallel and perpendicular to local background magnetic field, measured by FGM. Parallel heat flux is defined as following (Tong, Vasko, Artemyev, et al., 2019),

$$q_e = \frac{m_e}{2} \int \left(v_{\|} - \langle v_{\|} \rangle\right) (\boldsymbol{v} - \langle \boldsymbol{v} \rangle)^2 f(\boldsymbol{v})\, d^3\boldsymbol{v}$$

Here $f(\boldsymbol{v})$ is the electron velocity distribution function (VDF) and m_e is the electron mass. Figures 1f1–1f3 show the time series of electron temperature anisotropy (black curve) and normalized parallel heat flux (blue curve) for each corresponding event. The parallel heat flux is normalized with respect to the free-flowing heat flux, $q_0 = 1.5 n_e T_e (2T_e/m_e)^{1/2}$, where T_e is the electron temperature in energy units and n_e is electron number density (Tong, Vasko, Artemyev, et al., 2019). We also examine the relationship between whistler-mode wave amplitude and lunar crustal magnetic fields by identifying data points where background magnetic field line measured by the

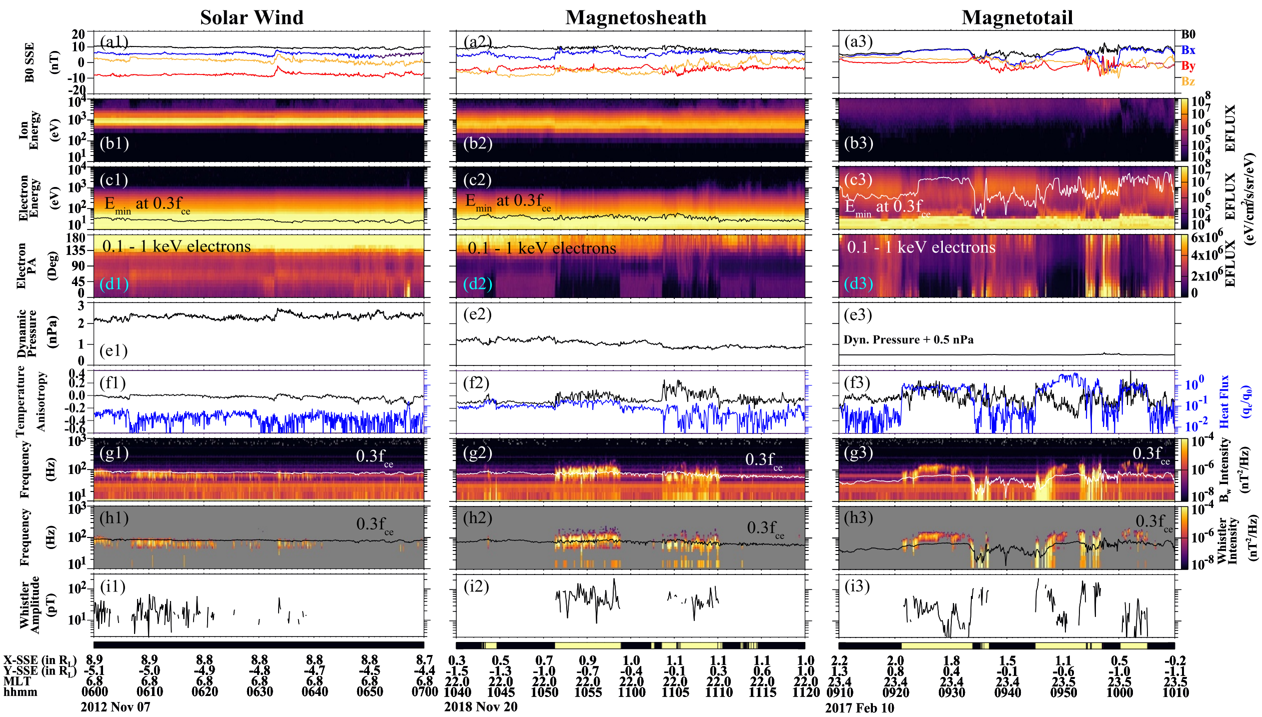

Figure 1. ARTEMIS observations of electrons and whistler-mode waves across different plasma regions: solar wind, magnetosheath, and magnetotail. (a1–a3) Background magnetic fields and their three components in SSE coordinates; (b1–b3) Energy spectrogram of ion energy flux; (c1–c3) Energy spectrogram of electron energy flux (black and white lines correspond to the minimum resonance energies for $0.3\,f_{ce}$ wave frequency); (d1–d3) Pitch angle spectrogram of electron energy flux for 0.1–1 keV electrons; (e1–e3) Dynamic pressure; (f1–f3) Temperature anisotropy (black) and normalized parallel heat flux (blue) for 10 eV–24 keV electrons; (g1–g3) Frequency spectrogram of magnetic wave intensity; (h1–h3) Frequency spectrogram of whistler-mode wave intensity after filtering; (i1–i3) Magnetic wave amplitudes of whistler-mode waves. The bars at the bottom of figure indicate the background magnetic field connection to the Moon (black: no connection; yellow: connection with field lines pointing away from the lunar surface; blue: connection with field lines pointing toward the surface).

probes is either connected or disconnected from the lunar surface. Magnetic field line connectivity to the lunar surface is determined by assuming a straight-line magnetic field from the probe location to the Moon along the direction of in-situ magnetic fields measured by the FGM instrument. The linear magnetic field line assumption has its limitations considering lunar crustal magnetic fields, the Parker spiral magnetic field configuration in the solar wind, or field line perturbation during interplanetary shocks. However, magnetic field connectivity to the lunar surface has a limited dependence on the exact magnetic field structure and the linear assumption serves as a reasonable approximation to the first order (Harada et al., 2014, 2015; Mitchell et al., 2008). The bars at the bottom of Figure 1 indicate the time periods when the magnetic field lines are connected or disconnected from the lunar surface for each event. The color bars indicate a first-order correlation between magnetic field connectivity and whistler-wave intensification in the magnetosheath and magnetotail observations. The in-situ measurements from FGM and ESA within the Moon's geometric shadow, extending up to 5 R_L (where R_L is the lunar radius), are excluded from this study due to significant uncertainties.

3. Global Distribution Maps of Whistler-Mode Waves

To investigate regions within the lunar plasma environment that are conductive to the generation of strong whistler-mode waves, we construct global distribution maps of wave amplitude and occurrence rate using 11 years of ARTEMIS data. These maps are developed in two coordinate systems: the Geocentric Solar Ecliptic (GSE) system, relative to Earth, and the Selenocentric Solar Ecliptic (SSE) system, relative to the Moon. In the GSE coordinate system, the positive X axis points from Earth toward the Sun, the Z axis is aligned with the northward normal to Earth's ecliptic plane, and the Y axis completes the orthogonal system. The SSE coordinate system is similar to the GSE system, but its origin is centered on the center of the Moon. The global maps are further categorized into different plasma regions encountered during a lunar orbit: solar wind, magnetosheath, and magnetotail. These regions are categorized based on the GSE longitude of the Moon (θ_{GSE}) relative to the positive

10.1029/2025JA033820

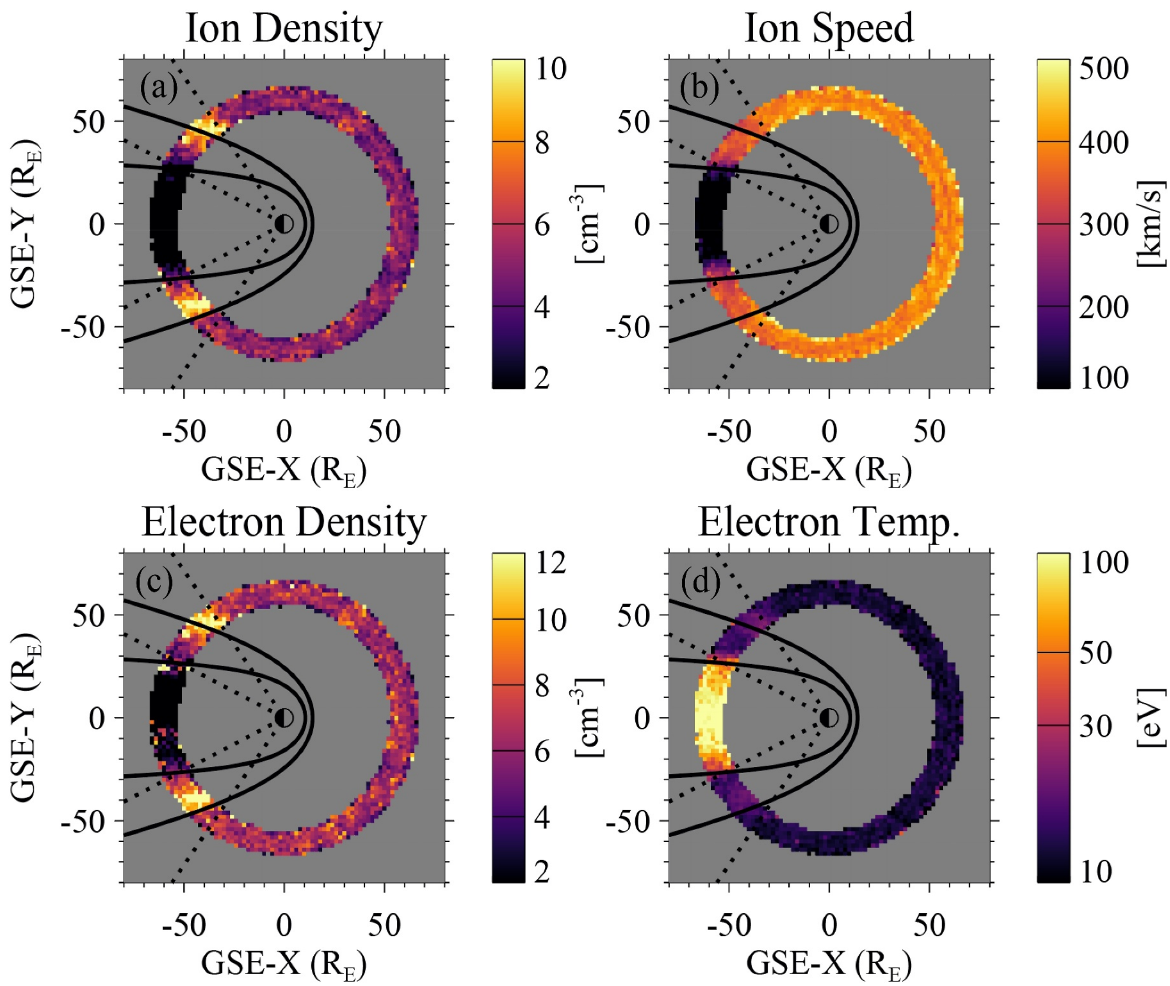

Figure 2. (a) Global distribution maps of average ion density, (b) ion speed, (c) electron density, and (d) electron temperature in GSE coordinates. The black dotted lines indicate the GSE longitudes of the Moon used for separating different plasma regions, while the black solid lines represent the modeled magnetopause and bow shock boundaries.

X-axis, as follows: solar wind: $\theta_{GSE} < 125°$ and $\theta_{GSE} > -125°$; magnetosheath: $125° < \theta_{GSE} < 153°$ or $-153° < \theta_{GSE} < -125°$; magnetotail: $\theta_{GSE} < -153°$ or $\theta_{GSE} > 153°$. The choice of these angular ranges is adapted from Sawaguchi et al. (2022) and is based on the global distribution maps of average ion and electron density, ion speed, and electron temperature, as shown in Figure 2. The spatial distribution of these parameters is shown in the GSE coordinate system, using a bin size of 2 R_E. In each panel of Figure 2, the black dotted lines indicate the GSE longitudes corresponding to the different plasma regions, as defined earlier. The black solid lines represent the boundaries of Earth's magnetopause and bow shock, calculated based on models (Chao et al., 2002; Shue et al., 1998; Wang et al., 2018) for southward magnetic field $B_Z = 0.0126$ nT, solar wind dynamic pressure of 1.73 nPa and magnetosonic mach number of 6. The southward magnetic field and dynamic pressure were obtained from NASA OMNI 1-min resolution data from 2010 through 2014 and the magnetosonic Mach number was obtained from Ma et al. (2020). Note that the separation criteria used to categorize different plasma regions, as described above are empirically determined based on the global distribution maps of average plasma parameters shown in Figure 2. They do not rely on modeled predictions of the magnetopause or bow-shock locations, which are included for illustrative purpose only. To further validate the separation criteria, we calculate the percentage of data points within each region which lie within the characteristic ranges of electron temperature and ion speed for the corresponding region. Specifically, in the solar wind, electron temperature should be below 50 eV and ion speed should exceed 250 km/s; in the magnetosheath, electron temperature should be below 200 eV and ion speed should exceed 200 km/s; and in the magnetotail, electron temperature should be above 20 eV. In the solar wind, magnetosheath, and magnetotail region, we found that 99.0%, 95.9% and 89.1% of data points,

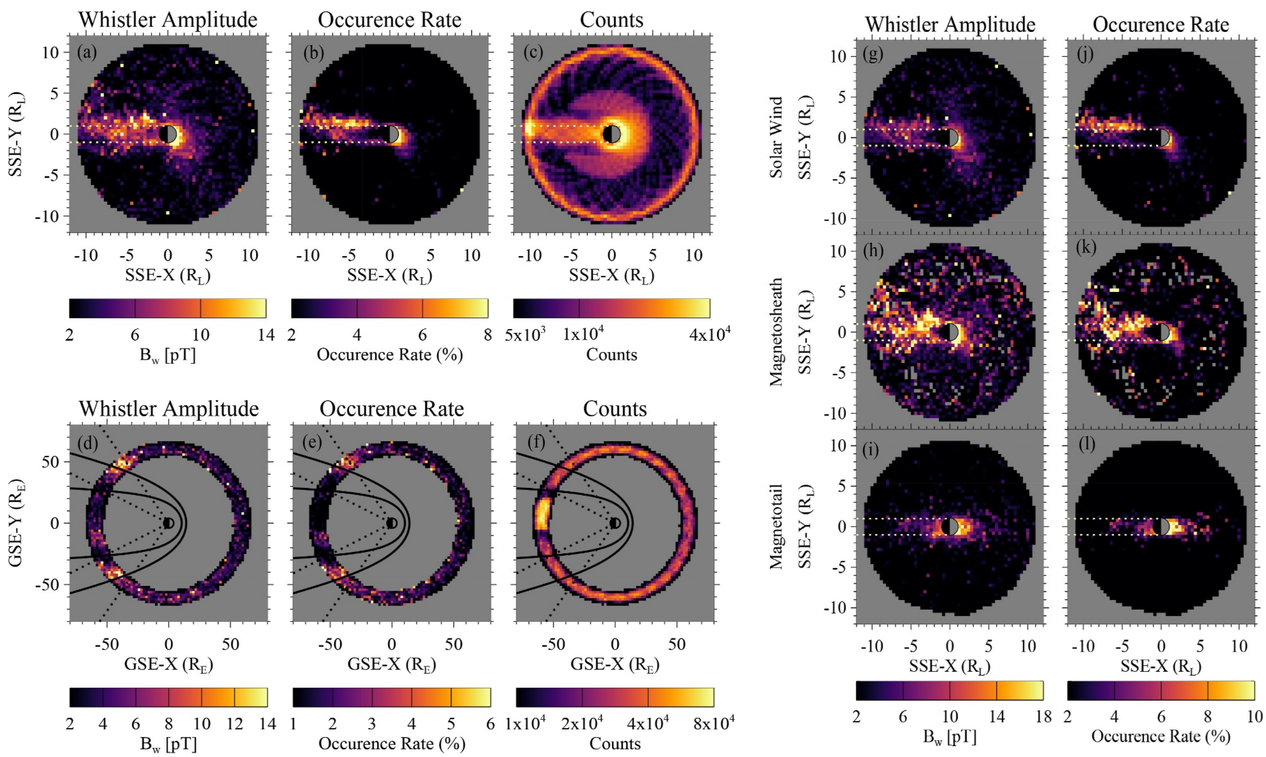

Figure 3. Global distribution maps of whistler-mode wave amplitude and occurrence rate. (a–c) Distribution of RMS wave amplitude, occurrence rate for events with amplitude >5 pT and data counts in SSE coordinates (centered on Moon); (d–f) distribution of RMS wave amplitude, occurrence rate, and data counts in GSE coordinates (centered on Earth); (g–i) distribution of RMS amplitude in SSE coordinates, categorized by different plasma regions; (j–l) distribution of occurrence rate in SSE coordinates, categorized by different plasma regions.

respectively, satisfied the corresponding criteria. With at least 85% data points lying within the expected range of parameters, these results demonstrate that the separation criteria based on GSE longitude of Moon provides a reliable approximation for identifying different plasma regions. It is noteworthy that with these separation criteria, there is always a possibility that the data points close to the boundaries of different plasma regions may be incorrectly categorized. However, we tested this by varying the GSE longitude thresholds for each region by ±3°, and no significant changes were observed in the overall results. The margin of ±3° is based on the approximate angular thickness of magnetopause or bow-shock boundaries highlighted by the transition in average ion and electron densities across different plasma regions (Figures 2a and 2c). This suggests that the adopted separation method provides a robust approximation for separating the different regions, with only minor errors due to potential misclassification of boundary data points.

Figure 3 shows the global distribution maps of whistler-mode wave amplitude and occurrence rate in both SSE and GSE coordinates. For each spatial bin, the whistler-mode wave amplitude is calculated as the Root Mean Square (RMS) wave amplitude, and the occurrence rate is defined as the percentage of data points with an amplitude larger than 5 pT. Figures 3a and 3b show the spatial distribution of amplitude and occurrence rate in SSE coordinate system with a bin size of 0.4 R_L (R_L is the lunar radius). Figures 3d and 3e show similar distributions in GSE coordinates. The black dashed and solid lines in Figures 3d–3f correspond to the boundaries shown in Figure 2. The global maps reveal that the solar side of the Moon exhibits high wave amplitude and occurrence rates close to the lunar surface (within 3–4 R_L), whereas the anti-solar side shows significant wave amplitudes and occurrence rates extending as far as 10 R_L (Figures 3a and 3b). Toward the flank regions, most whistler-mode events are confined within 2–3 R_L. Figures 3d and 3e show that whistler-mode wave amplitude and occurrence rate are highest when the Moon traverses Earth's magnetosheath.

Figures 3g–3l show the spatial distribution of wave amplitude and occurrence rate, respectively, in SSE coordinates, categorized by the different plasma regions encountered during a lunar orbit around the Earth. Across all the regions, we find high whistler-mode wave amplitudes on the dayside of the Moon within 2–3 R_L. In the solar wind, the occurrence rate drops significantly deep inside the lunar wake up to 5 R_L, with some occurrence rates observed around the boundary of geometric shadow of the Moon highlighted by white-dotted lines in Figure 3j. Similarly, the whistler-mode wave amplitudes on the anti-solar side drop inside wake extending up to 3 R_L (Figure 3g). Beyond 5 R_L on anti-solar side, high whistler-mode wave amplitude and occurrence rate are observed even deep within the lunar shadow (Figures 3g and 3j). This may be attributed to plasma flows beginning to refill the wake and merging from either side of the wake boundary, leading to the development of various instabilities beyond 5 R_L (Zhang et al., 2014). We also find an asymmetry in the whistler-mode wave occurrence rate between the dawn and dusk flanks when the Moon is in the solar wind (Figure 3j). This asymmetry could potentially result from asymmetric plasma flows around the dawn-dusk flank regions, leading to an asymmetric electron temperature anisotropy (see Supporting Information Figure S1 in Supporting Information S1 for more details). In the magnetosheath, the overall whistler-mode wave amplitude and occurrence rate are significantly higher compared to when the Moon is in the solar wind (Figures 3g, 3h, 3j and 3k). Moreover, on the anti-solar side, the reduction in wave amplitude and occurrence rate within the lunar wake only extends up to 1–2 R_L (Figures 3h and 3k). In the magnetotail, the distributions of whistler-mode wave amplitude and occurrence rate are much more symmetric between the solar and anti-solar sides, possibly due to the X-GSE aligned magnetic field and bi-directional plasma flows observed in the magnetotail (Figures 3i and 3l).

4. Dependence on Temperature Anisotropy and Parallel Heat Flux of Low- and High-Energy Electrons

Whistler-mode wave generation is strongly depedent on electron velocity distribution function, electron number density, and magnetic field strength (Gurnett & Bhattacharjee, 2017; Kennel, 1966). To investigate whistler-mode wave generation in the lunar plasma environment, we focus on a few plasma parameters that potentially play an important role. Specifically, we analyze electron temperature anisotropy ($T_{e\perp}/T_{e\parallel} - 1$), normalized parallel heat flux (q_e/q_0) and parallel plasma beta ($\beta_\parallel = 2\mu_0 n_e T_{e\parallel}/B_0^2$), where μ_0 is permeability of free space and B_0 is the background magnetic field. These parameters are analyzed to understand their correlation with whistler-mode wave amplitude and occurrence rate. When the Moon is in the solar wind and magnetosheath regions, we calculate these parameters for the entire electron population measured by the ESA instrument (approximately 10 eV–24 keV). However, for the magnetotail region, the measurements below the spacecraft potential (~30 eV) are excluded due to significant photoelectrons in the very low-energy channels.

Figure 4 shows 2D plots of whistler-mode wave occurrence rate as a function of various electron parameters, categorized by different plasma regions. The dotted and dashed lines represent theoretical parametric thresholds for different maximum growth rates (Gary et al., 1994, 2005). Note that the occurrence rate is calculated only for bins with at least 1,000 data points in order to have sufficiently low uncertainty. Throughout the paper the energy range labeled in panels corresponding to the magnetotail region has a lower limit of 30 eV rather than 10 eV, to reflect that electron populations below the spacecraft potential (typically above 10 V in the magnetotail) are not included in the calculation of electron moments. In general, across all the plasma regions, the highest occurrence rates are observed when the temperature anisotropy is greater than zero, corresponding to a transverse electron VDF favorable for whistler-mode wave generation (Figures 4a–4f). However, we observe a significant occurrence rate (~3%–10%) at negative anisotropies below −0.4 (corresponding to a field-aligned electron VDF) when the Moon is in the magnetosheath and magnetotail regions (Figures 4b and 4e, 4f). In contrast, normalized parallel heat flux does not exhibit a significant positive correlation with whistler-mode wave occurrence rate in the solar wind and magnetosheath regions (Figures 4d, 4e, 4g and 4h). It is worth noting that the overall trend of occurrence rate distribution in Figure 4g for the solar wind region closely resembles findings from a previous statistical study of quasi-parallel whistler-mode waves in the lunar plasma environment (Tong, Vasko, Artemyev, et al., 2019). In the magnetotail region, high occurrence rates are observed for normalized parallel heat flux above 0.1 (Figures 4f and 4i). In the solar wind and magnetosheath regions, most whistler-mode wave events occur when the parallel plasma beta is greater than 0.1. However, a significant occurrence rate is also observed at lower plasma beta (<0.1) in the magnetotail region, especially when temperature anisotropy is positive. This is likely due to the higher magnetic field strength within Earth's magnetosphere (Figures 4a–4c).

While macroscopic plasma parameters, such as electron temperature anisotropy, provide valuable insights into the critical conditions for generating strong whistler-mode waves in the lunar plasma environment, previous studies have noted that these parameters often fail to accurately represent the pitch angle anisotropy of electron VDF within specific energy ranges of electrons in cyclotron resonance with whistler-mode waves (Page

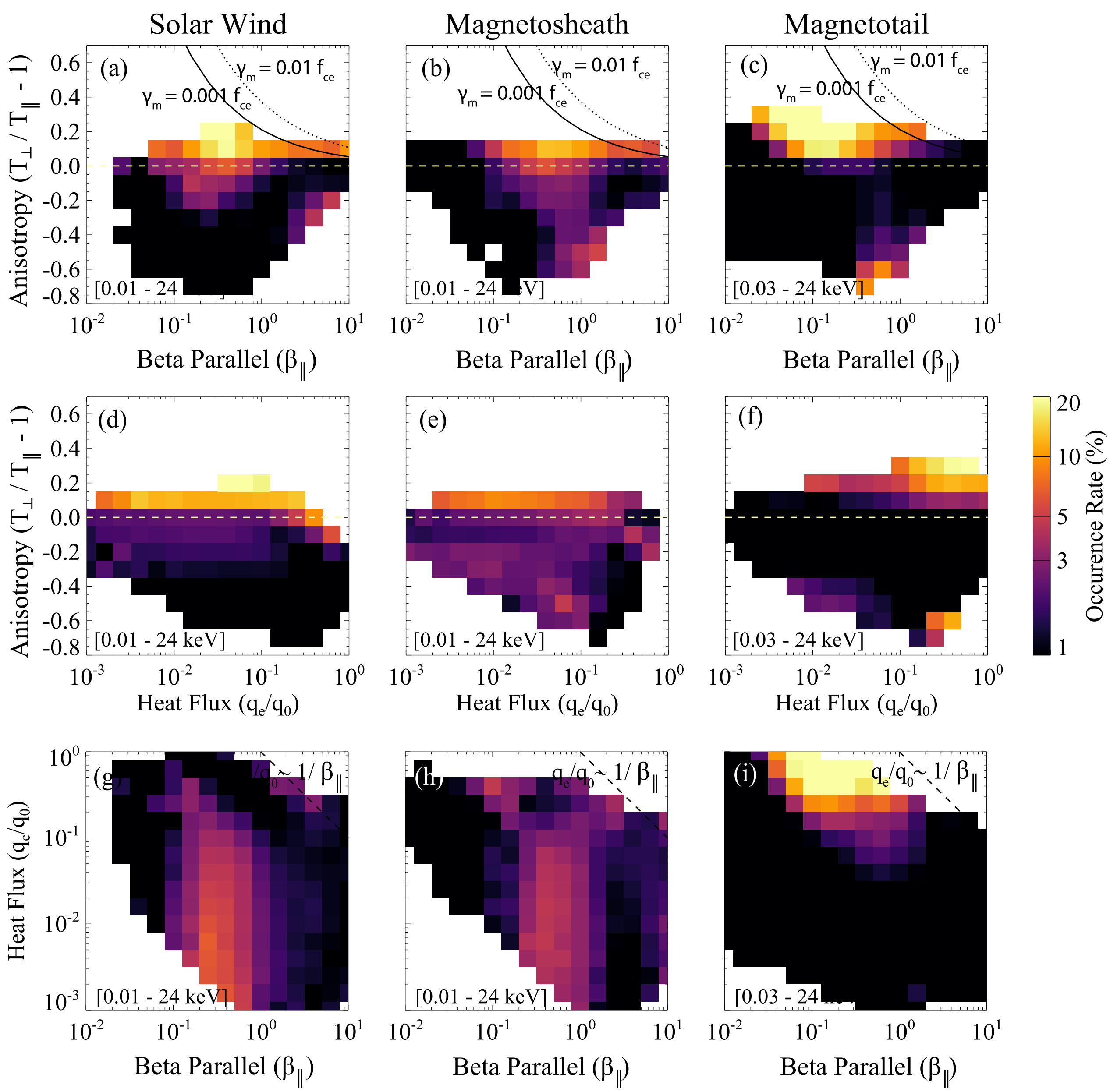

Figure 4. Distribution of whistler-mode wave occurrence rate in the solar wind, magnetosheath, and magnetotail. Occurrence rate as a function of (a–c) temperature anisotropy and parallel plasma beta; (d–f) temperature anisotropy and normalized parallel heat flux; (g–i) normalized parallel heat flux and parallel plasma beta. The energy range used for calculating the plasma parameters is indicated at the bottom left of each panel. In panels (a–c), the black solid and dashed lines represent the theoretical relationship between temperature anisotropy and parallel plasma beta for different values of maximum whistler-mode wave growth rates. In panels (g–i), the black dashed line corresponds to the theoretical relationship $q_e/q_0 \sim 1/\beta_{\parallel}$.

et al., 2021; Tong, Vasko, Pulupa, et al., 2019). To address this limitation, we calculated the electron particle moments separately for low-energy (<100 eV) and high-energy (>100 eV) electron populations. This categorization allows us to examine plasma parameters for different electron populations and their correlation with the whistler-mode wave occurrence rate.

Figure 5 shows line plots of whistler-mode wave occurrence rate and uncertainty as a function of electron temperature anisotropy and normalized parallel heat flux, calculated separately for high- and low-energy electron populations. The occurrence rate and uncertainty are calculated only for bins with at least 500 data points. Note that the normalization factor for parallel heat flux is calculated separately for each electron population, using the

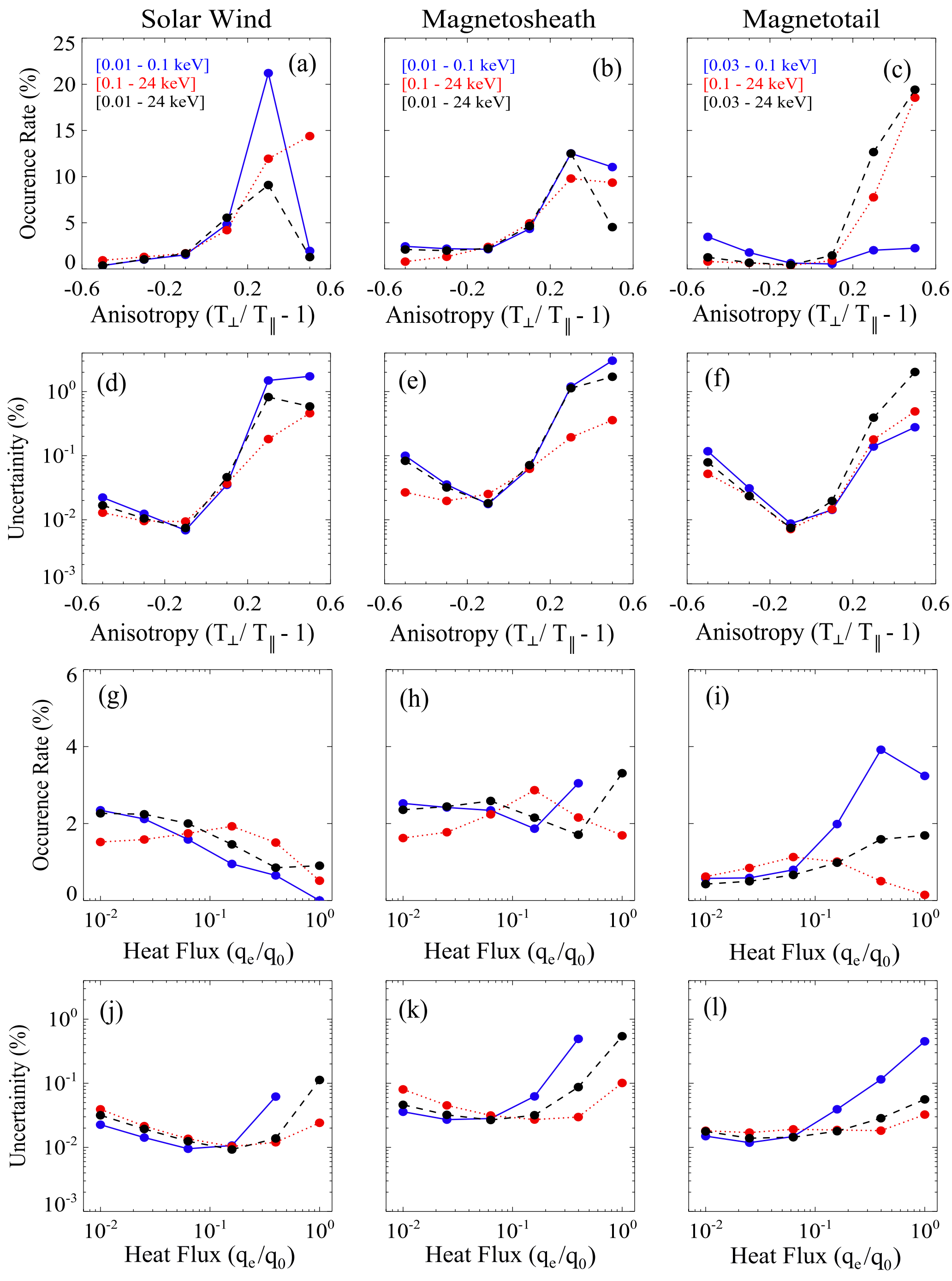

Figure 5. (a–c) Whistler-mode wave occurrence rate as a function of temperature anisotropy for low-energy electrons (blue), high-energy electrons (red), and all electrons combined (black) across different plasma regions; (d–f) uncertainty in occurrence rate as a function of temperature anisotropy; (g–i) occurrence rate as a function of normalized parallel heat flux for low-energy electrons (blue), high-energy electrons (red), and all electrons combined (black) across different plasma regions; (j–l) uncertainity in the occurrence rate as a function of normalized parallel heat flux. The energy range indicated in panels (a–c) correspond to the specific electron energy ranges used to calculate the plasma parameters for the line plots of the same color.

respective temperature and number density. The uncertainty is calculated as $\Delta = 2\sqrt{p(1-p)/n}$, where p is the occurrence rate and n is the data count. In the solar wind, the temperature anisotropy of the high-energy electron population shows a higher positive correlation with whistler-mode wave occurrence rate compared to that of low-energy population (Figure 5a). Conversely, normalized parallel heat flux for both low- and high-energy electron populations only exhibits a weak negative correlation with the occurrence rate in the solar wind (Figure 5g). In the magnetosheath, the electron temperature anisotropy of both low- and high-energy electrons exhibits a strong positive correlation with the occurrence rate (Figure 5b). However, the normalized parallel heat flux of either electron population does not exhibit a clear correlation, except for a slight increase in occurrence rate when the normalized parallel heat flux of the low-energy population exceeds 0.1 (Figure 5h). In the magnetotail region, a strong contrast is observed between the low- and high-energy electron populations. The temperature anisotropy of the high-energy electron population exhibits a strong positive correlation with the whistler-mode wave occurrence rate, whereas the temperature anisotropy of the low-energy population shows no positive correlation (see Figure 5c). This can be attributed to the fact that the minimum resonance energy for whistler-mode waves is typically higher in the magnetotail region. As a result, only the high-energy electron population can resonate with the waves, and their corresponding pitch angle anisotropy contributes to wave generation (see Figure 1c3 for reference). Figure 5i shows some positive correlation between the normalized parallel heat flux of low-energy electrons and the whistler-mode wave occurrence rate in the magnetotail region. This suggests that the high occurrence rate for normalized parallel heat flux above 0.1 in Figure 4i may be significantly influenced by low-energy electron population in the magnetotail. Overall, Figure 5 demonstrates that the whistler-mode wave occurrence rate is critically dependent on the temperature anisotropy of the high-energy (>100 eV) electron population across all the plasma regions. While the temperature anisotropy of low-energy (<100 eV) electron population is also important for whistler-mode wave generation in the solar wind and magnetosheath regions, it has little influence in the magnetotail. Additionally, no strong positive correlation is observed between normalized parallel heat flux for either low- or high-energy electron populations and the whistler-mode wave occurrence rate across the different plasma regions.

Figure 6 shows the normalized whistler-mode wave amplitude and occurrence rate as functions of temperature anisotropy and normalized parallel heat flux for low-energy (Figures 6a–6f) and high-energy (Figures 6g–6l) electrons. Bins with data counts below 1,000 in Figure 6 are left blank. The whistler-mode wave amplitude is normalized to the background magnetic field measured by the FGM instrument. In the solar wind and magnetosheath regions, increased normalized whistler-mode wave amplitude and occurrence rate are observed for positive temperature anisotropy of low- and high-energy electron populations, with a stronger correlation for high-energy electrons (Figure 6). This trend is consistent with the line plots shown in Figures 5a and 5b. By comparing Figure 4d with Figures 6d and 6j in the solar wind, we can infer that the occurrence rate observed at negative temperature anisotropy (below −0.1) in Figure 4d likely has more contributions from the low-energy electron population, which is not always in resonance with whistler-mode waves. Therefore, the low-energy population potentially plays a critical role in whistler-mode wave occurrence in the solar wind. Similarly, comparing Figure 4e with Figures 6e and 6k in the magnetosheath region suggests that the occurrence rate observed at temperature anisotropy below −0.4 in Figure 4e could be significantly influenced by the low-energy electron population. Additionally, a comparison of Figures 6a and 6g in the solar wind and Figures 6b and 6h in the magnetosheath shows significant whistler-mode wave amplitudes at negative temperature anisotropy for the low-energy electron population, indicating lower contributions to whistler-mode wave generation. These observations emphasize the importance of evaluating macroscopic plasma parameters for different energy populations separately. This approach provides improved insights into the electron populations that are critical for the generation of whistler-mode waves across various plasma regions.

In the solar wind region, the normalized whistler-mode wave amplitude shows a slight increase with higher normalized parallel heat flux at constant anisotropy levels of high-energy electron population (Figure 6g). However, this trend is not reflected in the occurrence rate (Figure 6j). Notably, a similar contrast between the correlation of normalized whistler-mode wave amplitude and occurrence rate in the solar wind was previously reported by Tong, Vasko, Artemyev, et al. (2019). They noted that the occurrence of whistler-mode waves is critically dependent on temperature anisotropy rather than heat flux or plasma beta. In the magnetosheath region, both the normalized whistler-mode wave amplitude and occurrence rate increase with higher normalized parallel heat flux of the high-energy electron population at constant anisotropy levels (Figures 6h and 6k). In the magnetotail region, the temperature anisotropy of the high-energy electron population is strongly correlated with both normalized whistler-mode wave amplitude and occurrence rate (Figures 6i and 6l), whereas the temperature anisotropy of low-energy electrons shows no correlation (Figures 6c and 6f). In contrast to the solar wind and magnetosheath regions, the normalized whistler-mode wave amplitude and occurrence rate in the magnetotail

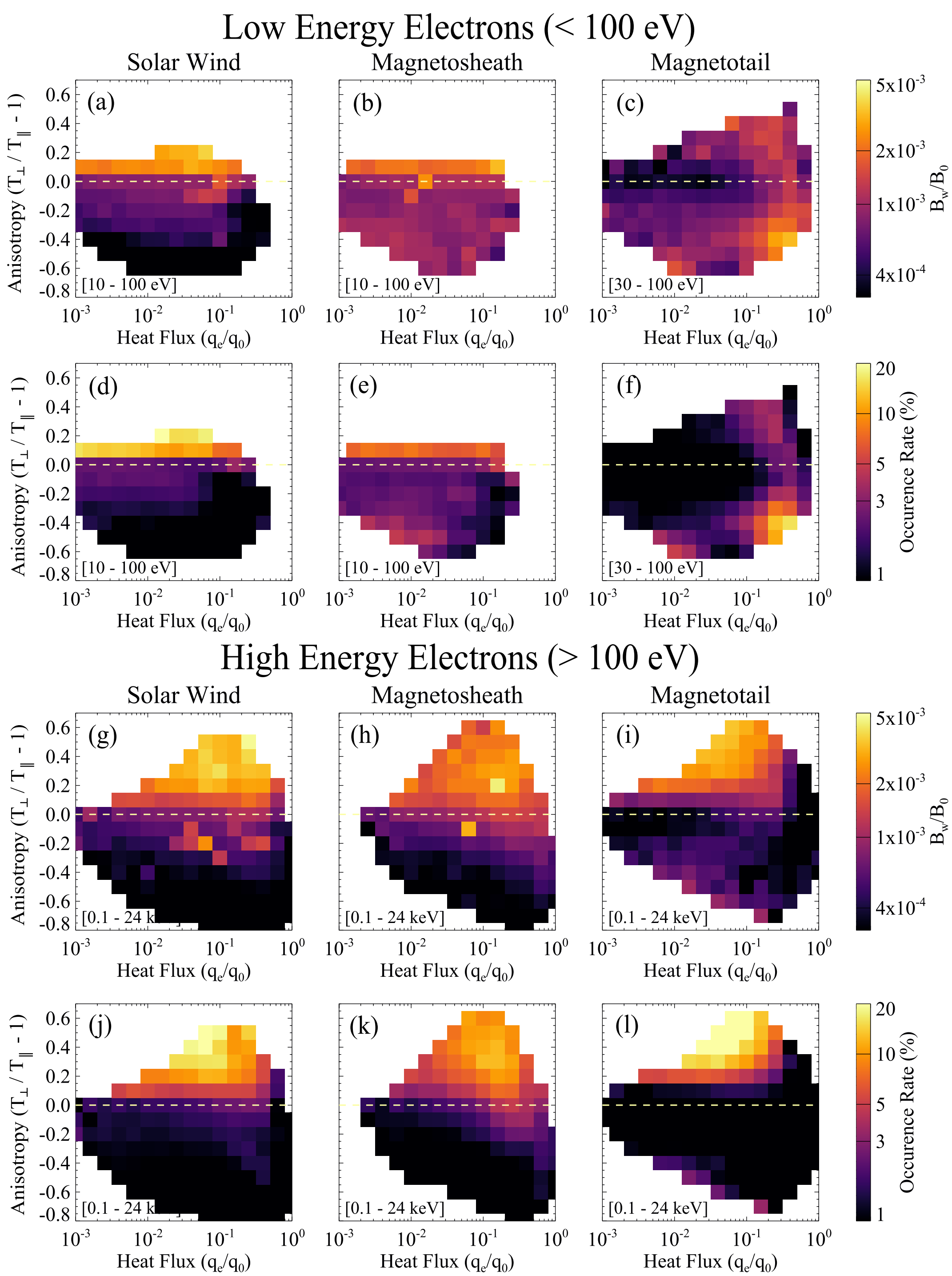

Figure 6. (a–f) Distribution of normalized whistler-mode wave amplitude and occurrence rate as a function of temperature anisotropy and normalized parallel heat flux for low-energy electrons, in the solar wind, magnetosheath and magnetotail; (g–l) similar to panels (a–f), but for high-energy electrons. The electron energy range indicated at the bottom left of each panel corresponds to the specific energy range used for calculating the plasma parameters.

region increase with higher normalized parallel heat flux of the low-energy electron population at constant anisotropy levels (Figures 6c and 6f). This could possibly be attributed to the fast plasma flows in the magnetotail, which can lead to an increased heat flux of the low-energy electron population, providing a free energy source for whistler-mode wave generation even if these electrons are not in resonance with the waves. Comparing Figure 4f

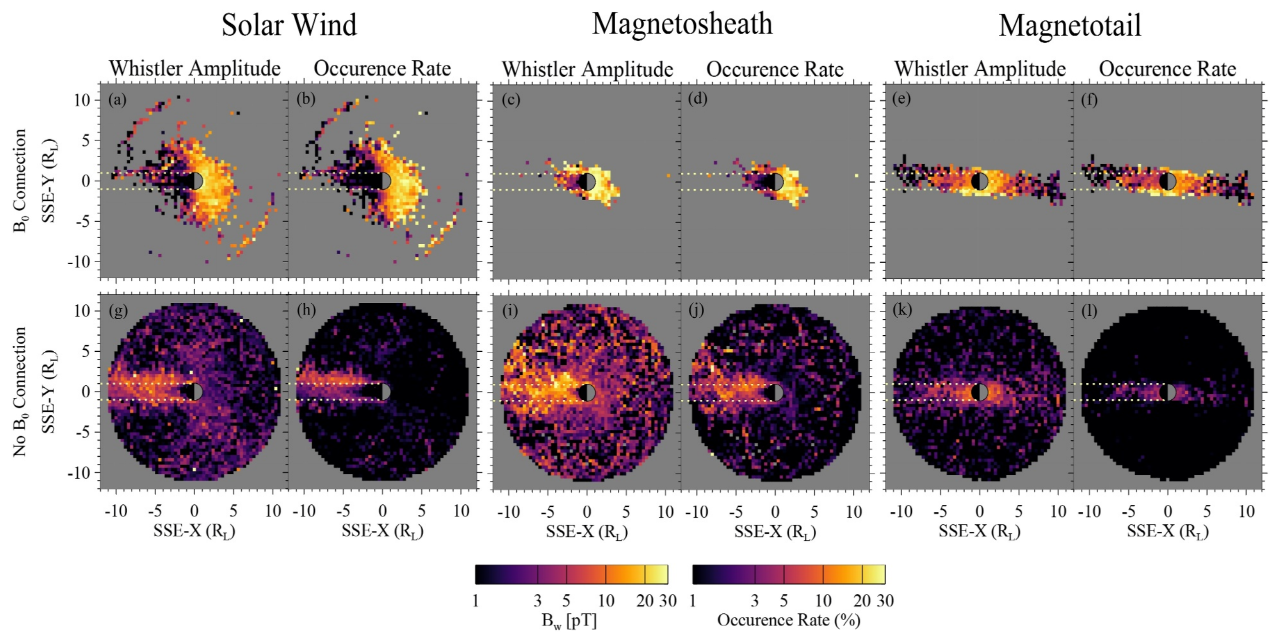

Figure 7. (a–f) Global distribution maps of RMS whistler-mode wave amplitude and occurrence rate for data points magnetically connected to the lunar surface, categorized by different plasma regions; (g–l) Corresponding distribution maps for data points magnetically disconnected from the lunar surface, categorized by different plasma regions.

with Figures 6f and 6l, it is evident that the occurrence rate observed at temperature anisotropy below −0.4 in Figure 4f is largely influenced by low-energy electron population that often does not resonate with whistler-mode waves. However, Figures 6f and 6l also show that a small occurrence rate (∼2%–3%) is observed when temperature anisotropy of the high-energy electron population is below −0.4. Additionally, a few events in the magnetotail region occur when the temperature anisotropy of both low- and high-energy electron populations is quite low (below −0.2). We suspect that some of these data points may be associated with other wave modes (see Section 6 and Supporting Information Figure S2 in Supporting Information S1 for further discussion).

In summary, we find that the electron temperature anisotropy of the high-energy electron population exhibits the strongest positive correlation with whistler-mode wave occurrence rate across different plasma regions. The temperature anisotropy of the low-energy electron population shows a significant positive correlation with whistler-mode wave occurrence rate in the solar wind and magnetosheath regions, yet no clear correlation in the magnetotail. In the solar wind and magnetosheath, the normalized parallel heat flux of the high-energy electron population shows some positive correlation with normalized whistler-mode wave amplitude. In contrast, in the magnetotail region it is the normalized parallel heat flux of low-energy electron population that exhibits some positive correlation with normalized wave amplitude.

5. Dependence on Magnetic Field Line Connection to the Lunar Surface

Strong whistler-mode waves in the vicinity of the Moon are often associated with crustal magnetic field sources distributed sporadically across the lunar surface (Harada et al., 2014, 2015; Sawaguchi et al., 2021, 2022). In this study, we utilize the 11-year ARTEMIS data set to develop global distribution maps of whistler-mode wave amplitude and occurrence rate, categorized into magnetically connected and disconnected cases across various plasma regions encountered during a lunar orbit. We assume the background magnetic field line is a straight line and extend it toward the Moon to determine its connection to the lunar surface. Additionally, we examine plasma parameters (electron temperature anisotropy and parallel heat flux) for magnetically connected and disconnected data points to assess the overall influence of lunar surface on the critical plasma parameters responsible for whistler-mode wave generation.

Figure 7 shows global distribution maps of whistler-mode wave amplitude and occurrence rate for different plasma regions, categorized into magnetically connected and disconnected cases. Across all plasma regions, the

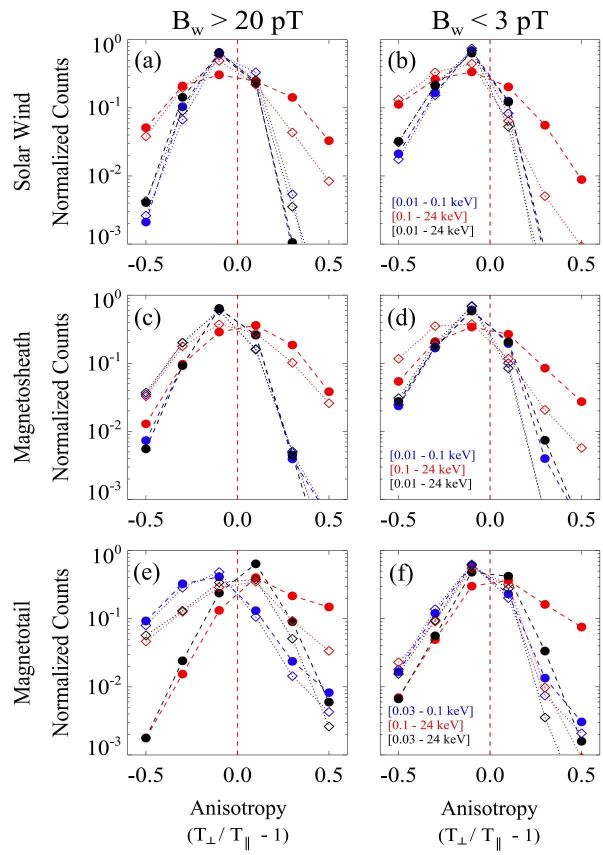

	SOLAR WIND			
	B_w > 20 pT		B_w < 3 pT	
	Connect (- - -)	No Connect (· · ·)	Connect (- - -)	No Connect (· · ·)
Ratio	0.760	0.377	0.368	0.075
Ratio	0.319	0.510	0.145	0.091
Ratio	0.295	0.349	0.139	0.056
Counts	52165	76892	526676	16302952

	MAGNETOSHEATH			
	B_w > 20 pT		B_w < 3 pT	
	Connect (- - -)	No Connect (· · ·)	Connect (- - -)	No Connect (· · ·)
Ratio	1.516	0.712	0.644	0.170
Ratio	0.359	0.201	0.250	0.112
Ratio	0.360	0.196	0.272	0.094
Counts	12660	36741	93543	3699057

	MAGNETOTAIL			
	B_w > 20 pT		B_w < 3 pT	
	Connect (- - -)	No Connect (· · ·)	Connect (- - -)	No Connect (· · ·)
Ratio	5.684	0.954	1.798	0.495
Ratio	0.205	0.149	0.331	0.270
Ratio	2.792	0.753	0.838	0.387
Counts	12412	8404	202052	5024150

Figure 8. (a, b) Distribution of normalized data counts as a function of temperature anisotropy for low-energy electrons (blue), high-energy electrons (red), and all electrons combined (black) categorized by high- and low-whistler-mode amplitudes. Dashed (dotted) curves correspond to data points with magnetic connection (disconnection) from the lunar surface; (c, d) corresponding panels for the magnetosheath region; (e, f) corresponding panels for the magnetotail region. The energy range specified in each panel refers to the specific energy range used to calculate the temperature anisotropy for the line plots of the corresponding colors. Table summarizes the ratio of the number of data points with anisotropy greater than zero to those with anisotropy less than zero for the respective categories. The total counts in each category, used to normalize the distributions, are also specified in the table.

whistler-mode wave amplitude and occurrence rate are significantly higher when magnetic field lines are connected to the lunar surface. For connected data points, the highest amplitudes and occurrence rates are observed on the solar side of the Moon (Figures 7a–7f). For disconnected data points, in the solar wind and magnetosheath regions, the highest amplitude and occurrence rate are observed on the anti-solar side and along the lunar wake boundary (Figures 7g–7j). In general, the magnetotail exhibits higher symmetry in wave amplitude and occurrence rate between the solar and anti-solar sides for both connected and disconnected data points (Figures 7e, 7f, 7k and 7l).

To investigate the strong whistler-mode waves observed when magnetic field lines are connected to the lunar surface, we analyze the electron temperature anisotropy for both low- and high-energy electron populations. These are categorized based on high (>20 pT) and low (<3 pT) whistler-mode wave amplitude, as well as whether the magnetic field lines are connected or disconnected to the lunar surface, as shown in Figure 8. Each panel in Figure 8 shows the normalized counts with respect to the temperature anisotropy of low-energy (blue), high-energy (red), and all electrons combined (black). The table shown in Figure 8 summarizes the ratio of the number of data points with anisotropy greater than zero compared to those with anisotropy less than zero. These ratios are calculated separately for different electron populations, as shown in colors corresponding to the respective line plots. A larger ratio reflects a higher percentage of data points with positive anisotropy for the given electron population and category. The correlation between temperature anisotropy and magnetic field line connection can be inferred by examining the changes in ratios across different categories. Across all plasma regions, the ratio of temperature anisotropy for the high-energy electron population increases as we move from disconnected to connected categories. For the low-energy electron population, the ratio also increases from

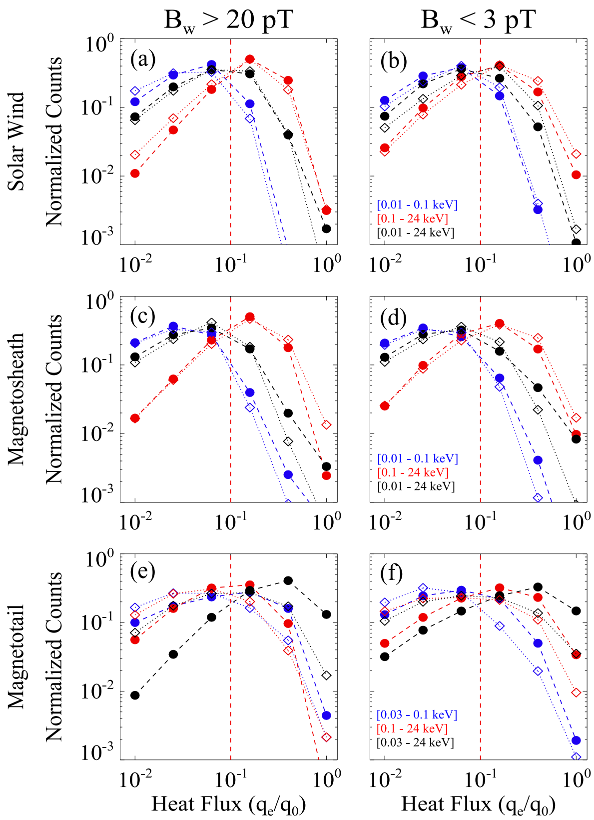

SOLAR WIND

	$B_w > 20$ pT		$B_w < 3$ pT	
	Connect (- - -)	No Connect (· · ·)	Connect (- - -)	No Connect (· · ·)
Ratio	3.086	2.182	1.428	2.088
Ratio	0.128	0.074	0.177	0.249
Ratio	0.535	0.609	0.467	1.013
Counts	52165	76892	526676	16302952

MAGNETOSHEATH

	$B_w > 20$ pT		$B_w < 3$ pT	
	Connect (- - -)	No Connect (· · ·)	Connect (- - -)	No Connect (· · ·)
Ratio	2.171	2.508	1.400	1.859
Ratio	0.045	0.026	0.074	0.052
Ratio	0.241	0.238	0.271	0.315
Counts	12660	36741	93543	3699057

MAGNETOTAIL

	$B_w > 20$ pT		$B_w < 3$ pT	
	Connect (- - -)	No Connect (· · ·)	Connect (- - -)	No Connect (· · ·)
Ratio	0.819	0.320	1.414	0.497
Ratio	0.794	0.281	0.377	0.123
Ratio	5.055	0.854	2.731	0.680
Counts	12412	8404	202052	5024150

Figure 9. (a, b) Distribution of normalized data counts as a function of normalized heat flux for low-energy electrons (blue), high-energy electrons (red), and all electrons combined (black) categorized by high- and low-whistler-mode amplitudes. Dashed (dotted) curves correspond to data points with magnetic connection (disconnection) from the lunar surface; (c, d) corresponding panels for the magnetosheath region; (e, f) corresponding panels for the magnetotail region. The energy range specified in each panel refers to the specific energy range used to calculate the temperature anisotropy for the line plots of the corresponding colors. Table summarizes the ratio of the number of data points with normalized heat flux greater than 0.1 to those with normalized heat flux less than 0.1 for the respective categories. The total counts in each category, used to normalize the distributions, are also specified in the table.

disconnected to connected categories when the Moon is in the magnetosheath and magnetotail region (see the Table in Figure 8). However, no clear correlation is observed for the low-energy electron population in solar wind region. The temperature anisotropy of the high-energy electron population shows a stronger response to magnetic field line connection to the lunar surface, likely indicating a more significant interaction with lunar crustal magnetic fields. Similar to Figure 8, we plot the normalized counts with respect to normalized parallel heat flux for different electron populations in Figure 9. The ratio represents the number of data points with normalized parallel heat flux greater than 0.1 compared to those with heat flux less than 0.1. In general, no clear correlation with normalized heat flux is observed across the connected and disconnected categories, except in the magnetotail region and solar wind region for high wave amplitude case, where the ratio for both high- and low-energy electron populations increases as we move from disconnected to connected categories (see the Table in Figure 9).

6. Discussion

Whistler-mode waves are among the most ubiquitously observed plasma waves in the vicinity of Earth's moon, and a number of studies have evaluated their generation using linear instability analysis based on locally measured electron distributions (Harada et al., 2014; Tong, Vasko, Pulupa, et al., 2019). Statistical studies have identified electron temperature anisotropy, parallel heat flux, and plasma beta as critical macroscopic plasma parameters for determining the growth rate of whistler-mode waves in the lunar plasma environment (Harada et al., 2015; Sawaguchi et al., 2022; Tong, Vasko, Artemyev, et al., 2019). However, it has been shown that macroscopic plasma parameters often fail to accurately capture electron pitch angle anisotropy of the electron populations in cyclotron resonance with whistler-mode waves, which are directly responsible for their generation (Page et al., 2021; Tong, Vasko, Pulupa, et al., 2019). In this study, we attempt to address this gap by building upon previous literature to analyze critical plasma parameters, such as temperature anisotropy and parallel heat flux, for low-energy (<100 eV) and high-energy (>100 eV) electron populations separately. The results reveal a strong contrast in the correlation of plasma parameters with whistler-mode waves for low- and high-energy electrons. For example, the temperature anisotropy of high-energy electrons generally shows a stronger positive correlation with whistler-mode wave occurrence rate compared to that of low-energy electrons (Figure 6). Similarly, the normalized parallel heat flux of high-energy electrons exhibits some positive correlation with normalized whistler-mode wave amplitude in the solar wind and magnetosheath regions, whereas the low-energy population does show such a feature in the magnetotail (Figure 6). The intensity of whistler-mode waves in the lunar plasma environment is well known to be strongly dependent on the presence of lunar magnetic field anomalies, which can reflect electrons, creating local electron pitch angle anisotropy favorable for whistler-mode wave generation (Halekas et al., 2006, 2012; Harada et al., 2014, 2015; Sawaguchi et al., 2022). In this study, we have demonstrated that the temperature anisotropy of the high-energy electron population exhibits a much stronger response to magnetic field line connection with the lunar surface compared to that of low-energy electrons (Figure 8).

In this statistical study, we used the magnetic wave spectra from the fast survey mode of SCM to identify whistler-mode waves, acknowledging its limitations in clearly distinguishing between different wave modes. The selection criteria for whistler-mode wave events, adapted from previous studies, provide a reliable approximation but are not entirely error-free. For example, in the magnetotail region, we identified a few wave events associated with field-aligned electron distribution across all ESA energy channels, accompanied by strong intensification in the magnetic spectra. We suspect that these events may be related to Kinetic Alfven Waves (KAW), rather than whistler-mode waves. An example of such event is shown in Supporting Information Figure S2 in Supporting Information S1, where KAW-like wave intensification is observed at 18:40 UT. To differentiate between the two types of intensifications and potentially exclude KAW-like events, we attempted to analyze electric spectra from the Electric Field Instrument (EFI) onboard ARTEMIS. However, the electric spectra did not reveal clear distinctive features from the whistler-like intensification observed at 18:25 UT (see Figure S2 in Supporting Information S1). Despite this, the number of data points corresponding to KAW-like events is small and is unlikely to significantly affect the statistical results of the present study.

7. Conclusions

In this study, we present comprehensive global maps of whistler-mode wave distribution and explore the underlying generation mechanisms in the lunar plasma environment, utilizing 11 years of ARTEMIS data. The key results and conclusions are summarized as follows.

1. Global distribution maps of whistler-mode wave amplitude and occurrence rate with respect to the Moon reveal that some of the strongest whistler-mode waves are detected on the solar side of the Moon, within 1–2 R_L.
2. Among the various plasma regions encountered during a lunar orbit, the highest RMS whistler-mode wave amplitude and occurrence rate are observed when the Moon crosses Earth's magnetosheath.
3. The distribution of whistler-mode wave amplitude and occurrence rate is more symmetric between the solar and anti-solar side of the Moon when it crosses Earth's magnetotail. In contrast, in the solar wind and magnetosheath regions, the RMS whistler-mode wave amplitude drops significantly deep inside the lunar wake extending up to 4 R_L and 2 $R_{L,}$ respectively.
4. Whistler-mode wave occurrence rate exhibits a strong positive correlation with the temperature anisotropy of the high-energy electron population across all the plasma regions encountered during a lunar orbit. The temperature anisotropy of low-energy electron populations also exhibits a weak positive correlation with whistler-mode wave intensity in the solar wind and magnetosheath regions.
5. When the Moon is in the solar wind and magnetosheath regions, the normalized parallel heat flux of high-energy electrons exhibits a positive correlation with the average normalized whistler-mode wave amplitude at constant anisotropy levels. In contrast, in the magnetotail region, the normalized parallel heat flux of low-energy electrons exhibits a positive correlation with the average normalized whistler-mode wave amplitude.
6. In the solar wind and magnetosheath regions, magnetic field line connection to the solar side of the lunar surface leads to stronger whistler-mode waves compared to connections on the anti-solar side of the Moon. In the magnetotail region, magnetic field line connections to both the solar and anti-solar sides of the Moon result in comparable whistler-mode amplitudes and occurrence rates.

7. Across all the plasma regions encounrtered during a lunar orbit, the temperature anisotropy of the high-energy electron population exhibits a stronger positive correlation with magnetic field line connection compared to that of low-energy electrons.

The Moon serves as a natural laboratory for studying plasma waves around airless planetary objects. In this study we investigate the generation of whistler-mode waves in lunar plasma environment which provided important insights on the contrasting importance of low- and high-electron population for wave generation, when the Moon is in the solar wind and Earth's magnetosphere. Global distribution maps of whistler-mode waves reveal the regions around the Moon favorable for strong wave generation and highlight the potential sources of large anisotropy of electrons. In future studies, it will also be interesting to study the global distribution of kinetic scale parameters critical for whistler-mode wave generation, such as the pitch angle anisotropy for low- and high-energy electron population.

Data Availability Statement

ARTEMIS data is publicly available at https://artemis.igpp.ucla.edu/ or NASA Space Physics Data Facility (SPDF) via Vassilis Angelopoulos, Bonnell, et al., 2023a, 2023b; Vassilis Angelopoulos, Carlson, et al., 2023a, 2023b; Vassilis Angelopoulos & Roux, 2023a, 2023b. The data used to produce figures in the present study are publicly available in figshare via https://doi.org/10.6084/m9.figshare.28182980.

Acknowledgments
AP would like to acknowledge the FINESST award 80NSSC24K1864. WL, QM, XS and MQ acknowledge the NASA Grants 80NSSC23K0410, 80NSSC22K1638, 80NSSC23K0096, 80NSSC24K0239, 80NSSC24K0572, and 80NSSC25K7686 and NSF Grants AGS-1847818, AGS-2225445 and AGS-2247774. AA would like to acknowledge NASA HGI 80NSSC21K0581. The authors acknowledge NASA contract NAS5-02099 for use of data from the THEMIS/ARTEMIS Mission. Specifically, we acknowledge the late C. W. Carlson and J. P. McFadden for use of ESA data, J. W. Bonnell and F. S. Mozer for use of EFI data, O. LeContel and the late A. Roux for use of SCM data and K. H. Glassmeier, F. Plaschke, U. Auster and W. Baumjohann for the use of FGM data.

References

Angelopoulos, V. (2011). The ARTEMIS mission. *Space Science Reviews*, *165*(1), 3–25. https://doi.org/10.1007/s11214-010-9687-2

Angelopoulos, V., Bonnell, J. W., & Mozer, F. S. (2023a). THEMIS-B (P1/ARTEMIS-P1), electric field instrument (EFI) spacecraft measured electric field. *NASA Space Physics Data Facility*. [Dataset]. https://doi.org/10.48322/HADN-2T57

Angelopoulos, V., Bonnell, J. W., & Mozer, F. S. (2023b). THEMIS-C (P2/ARTEMIS-P2), electric field instrument (EFI) spacecraft measured electric field. *NASA Space Physics Data Facility*. [Dataset]. https://doi.org/10.48322/GMR7-8198

Angelopoulos, V., Carlson, C. W., & McFadden, J. P. (2023a). THEMIS-B: ESA electron/ion energy fluxes and moments. *NASA Space Physics Data Facility*. [Dataset]. https://doi.org/10.48322/7G3T-F085

Angelopoulos, V., Carlson, C. W., & McFadden, J. P. (2023b). THEMIS-C: ESA electron/ion energy fluxes and moments. *NASA Space Physics Data Facility*. [Dataset]. https://doi.org/10.48322/SCC7-MJ94

Angelopoulos, V., & Roux, A. (2023a). THEMIS-B: Search Coil magnetometer 1/8s, 1/128s and 1/8192s data. *NASA Space Physics Data Facility*. [Dataset]. https://doi.org/10.48322/RWCH-KK19

Angelopoulos, V., & Roux, A. (2023b). THEMIS-C: Search Coil magnetometer 1/8s, 1/128s and 1/8192s data. *NASA Space Physics Data Facility*. [Dataset]. https://doi.org/10.48322/DW9H-K139

Auster, H. U., Glassmeier, K. H., Magnes, W., Aydogar, O., Baumjohann, W., Constantinescu, D., et al. (2008). The THEMIS fluxgate magnetometer. *Space Science Reviews*, *141*(1), 235–264. https://doi.org/10.1007/s11214-008-9365-9

Chao, J. K., Wu, D. J., Lin, C.-H., Yang, Y.-H., Wang, X. Y., Kessel, M., et al. (2002). Models for the size and shape of the earth's magnetopause and bow shock. In L.-H. Lyu (Ed.), *COSPAR colloquia series* (Vol. 12, pp. 127–135). Pergamon. https://doi.org/10.1016/S0964-2749(02)80212-8

Chu, F., Halekas, J. S., Cao, X., McFadden, J. P., Bonnell, J. W., & Glassmeier, K.-H. (2021). Electrostatic waves and electron heating observed over lunar crustal magnetic anomalies. *Journal of Geophysical Research: Space Physics*, *126*(4), e28880. https://doi.org/10.1029/2020JA028880

Fatemi, S., Holmström, M., Futaana, Y., Barabash, S., & Lue, C. (2013). The lunar wake current systems. *Geophysical Research Letters*, *40*(1), 17–21. https://doi.org/10.1029/2012GL054635

Gary, S. P., Lavraud, B., Thomsen, M. F., Lefebvre, B., & Schwartz, S. J. (2005). Electron anisotropy constraint in the magnetosheath: Cluster observations. *Geophysical Research Letters*, *32*(13), 2005GL023234. https://doi.org/10.1029/2005GL023234

Gary, S. P., Scime, E. E., Phillips, J. L., & Feldman, W. C. (1994). The whistler heat flux instability: Threshold conditions in the solar wind. *Journal of Geophysical Research*, *99*(A12), 23391–23399. https://doi.org/10.1029/94JA02067

Gurnett, D. A., & Bhattacharjee, A. (2017). *Introduction to plasma Physics: With space, laboratory and astrophysical applications* (2nd ed.). Cambridge University Press. https://doi.org/10.1017/9781139226059

Halekas, J. S., Bale, S. D., Mitchell, D. L., & Lin, R. P. (2005). Electrons and magnetic fields in the lunar plasma wake. *Journal of Geophysical Research*, *110*(A7), A07222. https://doi.org/10.1029/2004JA010991

Halekas, J. S., Brain, D. A., Mitchell, D. L., & Lin, R. P. (2006). Whistler waves observed near lunar crustal magnetic sources. *Geophysical Research Letters*, *33*(22), L22104. https://doi.org/10.1029/2006GL027684

Halekas, J. S., Mitchell, D. L., Lin, R. P., Hood, L. L., Acuña, M. H., & Binder, A. B. (2002). Evidence for negative charging of the lunar surface in shadow. *Geophysical Research Letters*, *29*(10), 1–77. https://doi.org/10.1029/2001GL014428

Halekas, J. S., Poppe, A., Delory, G. T., Farrell, W. M., & Horányi, M. (2012). Solar wind electron interaction with the dayside lunar surface and crustal magnetic fields: Evidence for precursor effects. *Earth Planets and Space*, *64*(2), 73–82. https://doi.org/10.5047/eps.2011.03.008

Halekas, J. S., Saito, Y., Delory, G. T., & Farrell, W. M. (2011). New views of the lunar plasma environment. *Planetary and Space Science*, *59*(14), 1681–1694. https://doi.org/10.1016/j.pss.2010.08.011

Harada, Y., & Halekas, J. S. (2016). Upstream waves and particles at the moon. In A. Keiling, D.-H. Lee, & V. Nakariakov (Eds.), *Geophysical monograph series* (pp. 307–322). John Wiley and Sons, Inc. https://doi.org/10.1002/9781119055006.ch18

Harada, Y., Halekas, J. S., Poppe, A. R., Kurita, S., & McFadden, J. P. (2014). Extended lunar precursor regions: Electron-wave interaction. *Journal of Geophysical Research: Space Physics*, *119*(11), 9160–9173. https://doi.org/10.1002/2014JA020618

Harada, Y., Halekas, J. S., Poppe, A. R., Tsugawa, Y., Kurita, S., & McFadden, J. P. (2015). Statistical characterization of the foremoon particle and wave morphology: ARTEMIS observations. *Journal of Geophysical Research: Space Physics*, *120*(6), 4907–4921. https://doi.org/10.1002/2015JA021211

Kennel, C. (1966). Low-frequency whistler mode. *The Physics of Fluids*, *9*(11), 2190–2202. https://doi.org/10.1063/1.1761588

Ma, X., Nykyri, K., Dimmock, A., & Chu, C. (2020). Statistical study of solar wind, magnetosheath, and magnetotail plasma and field properties: 12+ years of THEMIS observations and MHD simulations. *Journal of Geophysical Research: Space Physics*, *125*(10), e2020JA028209. https://doi.org/10.1029/2020JA028209

McFadden, J. P., Carlson, C. W., Larson, D., Ludlam, M., Abiad, R., Elliott, B., et al. (2008). The THEMIS ESA plasma instrument and in-flight calibration. *Space Science Reviews*, *141*(1), 277–302. https://doi.org/10.1007/s11214-008-9440-2

Mitchell, D. L., Halekas, J. S., Lin, R. P., Frey, S., Hood, L. L., Acuña, M. H., & Binder, A. (2008). Global mapping of lunar crustal magnetic fields by Lunar Prospector. *Icarus (New York, N. Y. 1962)*, *194*(2), 401–409. https://doi.org/10.1016/j.icarus.2007.10.027

Nakagawa, T. (2016). ULF/ELF waves in near-moon space. In A. Keiling, D.-H. Lee, & V. Nakariakov (Eds.), *Geophysical monograph series* (pp. 293–306). John Wiley and Sons, Inc. https://doi.org/10.1002/9781119055006.ch17

Nakagawa, T., & Iizima, M. (2005). Pitch angle diffusion of electrons at the boundary of the lunar wake. *Earth Planets and Space*, *57*(9), 885–894. https://doi.org/10.1186/BF03351866

Omura, Y. (2021). Nonlinear wave growth theory of whistler-mode chorus and hiss emissions in the magnetosphere. *Earth Planets and Space*, *73*(1), 95. https://doi.org/10.1186/s40623-021-01380-w

Omura, Y., Katoh, Y., & Summers, D. (2008). Theory and simulation of the generation of whistler-mode chorus. *Journal of Geophysical Research*, *113*(A4), A04223. https://doi.org/10.1029/2007JA012622

Page, B., Vasko, I. Y., Artemyev, A. V., & Bale, S. D. (2021). Generation of high-frequency whistler waves in the earth's quasi-perpendicular bow shock. *The Astrophysical Journal Letters*, *919*(2), L17. https://doi.org/10.3847/2041-8213/ac2748

Roux, A., Le Contel, O., Coillot, C., Bouabdellah, A., de la Porte, B., Alison, D., et al. (2008). The Search Coil magnetometer for THEMIS. *Space Science Reviews*, *141*(1), 265–275. https://doi.org/10.1007/s11214-008-9455-8

Sawaguchi, W., Harada, Y., & Kurita, S. (2021). Discrete rising tone elements of whistler-mode waves in the vicinity of the moon: ARTEMIS observations. *Geophysical Research Letters*, *48*(1), e2020GL091100. https://doi.org/10.1029/2020GL091100

Sawaguchi, W., Harada, Y., Kurita, S., & Nakamura, S. (2022). Spectral properties of whistler-mode waves in the vicinity of the moon: A statistical study with ARTEMIS. *Journal of Geophysical Research: Space Physics*, *127*(9), e2022JA030582. https://doi.org/10.1029/2022JA030582

Shue, J.-H., Song, P., Russell, C. T., Steinberg, J. T., Chao, J. K., Zastenker, G., et al. (1998). Magnetopause location under extreme solar wind conditions. *Journal of Geophysical Research*, *103*(A8), 17691–17700. https://doi.org/10.1029/98JA01103

Tong, Y., Vasko, I. Y., Artemyev, A. V., Bale, S. D., & Mozer, F. S. (2019). Statistical Study of Whistler Waves in the Solar Wind at 1 au. *The Astrophysical Journal*, *878*(1), 41. https://doi.org/10.3847/1538-4357/ab1f05

Tong, Y., Vasko, I. Y., Pulupa, M., Mozer, F. S., Bale, S. D., Artemyev, A. V., & Krasnoselskikh, V. (2019). Whistler wave generation by halo electrons in the solar wind. *The Astrophysical Journal*, *870*(1), L6. https://doi.org/10.3847/2041-8213/aaf734

Tsugawa, Y., Terada, N., Katoh, Y., Ono, T., Tsunakawa, H., Takahashi, F., et al. (2011). Statistical analysis of monochromatic whistler waves near the Moon detected by Kaguya. *Annales Geophysicae*, *29*(5), 889–893. https://doi.org/10.5194/angeo-29-889-2011

Wang, J., Guo, Z., Ge, Y. S., Du, A., Huang, C., & Qin, P. (2018). The responses of the earth's magnetopause and bow shock to the IMF B_z and the solar wind dynamic pressure: A parametric study using the AMR-CESE-MHD model. *Journal of Space Weather and Space Climate*, *8*, A41. https://doi.org/10.1051/swsc/2018030

Xu, S., Poppe, A. R., Halekas, J. S., Mitchell, D. L., McFadden, J. P., & Harada, Y. (2019). Mapping the lunar wake potential structure with ARTEMIS data. *Journal of Geophysical Research: Space Physics*, *124*(5), 3360–3377. https://doi.org/10.1029/2019JA026536

Xu, X., Xu, Q., Chang, Q., Xu, J., Wang, J., Wang, Y., et al. (2019). ARTEMIS observations of well-structured lunar wake in subsonic plasma flow. *The Astrophysical Journal*, *881*(1), 76. https://doi.org/10.3847/1538-4357/ab2e0a

Zhang, H., Khurana, K. K., Kivelson, M. G., Angelopoulos, V., Wan, W. X., Liu, L. B., et al. (2014). Three-dimensional lunar wake reconstructed from ARTEMIS data. *Journal of Geophysical Research: Space Physics*, *119*(7), 5220–5243. https://doi.org/10.1002/2014JA020111